

Stellar X-rays and magnetic activity in 3D MHD coronal models

J. Zhuleku, J. Warnecke and H. Peter

Max Planck Institute for Solar System Research, 37077 Göttingen, Germany
e-mail: zhuleku@mps.mpg.de

Received/Accepted

ABSTRACT

Context. Observations suggest a power-law relation between the coronal emission in X-rays, L_X , and the total (unsigned) magnetic flux at the stellar surface, Φ . The physics basis for this relation is poorly understood.

Aims. We use 3D MHD numerical models of the coronae above active regions, i.e. strong concentrations of magnetic field, to investigate the L_X vs. Φ relation and supply this by an analytical model based on simple well-established scaling relations.

Methods. In the 3D MHD model horizontal (convective) motions near the surface induce currents in the coronal magnetic field that are dissipated and heat the plasma. This self-consistently creates a million Kelvin hot corona. We run a series of models that differ by the (unsigned) magnetic flux at the surface by changing the (peak) magnetic field strength while keeping all other parameters fixed.

Results. In the 3D MHD models we find that the energy input into the corona, characterized by either the Poynting flux or the total volumetric heating, scales roughly quadratically with the unsigned surface flux Φ . This is expected from heating through field-line braiding. Our central result is the non-linear scaling of the X-ray emission as $L_X \propto \Phi^{3.44}$. This scaling is a bit steeper than found in recent observations that give power-law indices of only up to 2 or 3. Assuming that on a real star not only the peak magnetic field strength in the active regions changes but also their number (or surface filling factor), our results can be consistent with observations.

Conclusions. With our model, we give indications of an understanding of what causes the steep increase of the X-ray luminosity by four orders of magnitude from solar-type activity to fast rotating active stars.

Key words. Sun: corona - stars: coronae- magnetohydrodynamics (MHD) - methods: numerical - X-rays: stars

1. Introduction

Stellar coronal X-ray emission is observed to increase with stellar rotation rate (e.g. [Pizzolato et al. 2003](#); [Reiners et al. 2014](#)). It is widely assumed that an increase in rotation could be responsible for stronger dynamo action leading to larger surface magnetic field. Some active stars (e.g. M dwarfs) that rotate rapidly (typical periods of 1 to 2 days) show high (average) photospheric magnetic field strengths which can reach up to 8 kG or even more ([Reiners 2012](#)). Because of this increased photospheric magnetic field, we can expect that a stronger upward directed Poynting flux is generated that can heat the corona to higher temperatures and leads to stronger X-ray emission in the corona. An indication of such a behaviour has been found in stellar observations (e.g. [Vidotto et al. 2014](#)) revealing a close relation of the coronal X-ray emission and the surface magnetic flux.

The scaling relationship between the coronal X-ray emission L_X and the surface magnetic flux Φ , have been extensively studied by employing solar and stellar observations. This relation follows a power-law, $L_X \propto \Phi^m$. In early studies, the power-law index m was found to be close to unity ([Fisher et al. 1998](#); [Pevtsov et al. 2003](#)), i.e. the X-ray radiation scales almost linear with magnetic flux. However, more recent studies suggest a much steeper power law with $m = 1.80$ ([Vidotto et al. 2014](#)) or even steeper with $m = 2.68$ ([Kochukhov et al. 2020](#)). The physical mechanism relating the observed X-ray emission to the surface magnetic flux is still under debate.

To study the impact of the surface magnetic field on the coronal X-ray emission in the environment of a realistic setup, the use of 3D magnetohydrodynamic (MHD) models is required. In addition, the 3D numerical simulations will provide a useful tool

to further test the validity of a simplified analytical model. The main advantage of 3D models is the self-consistent treatment of the corona. The heating originates from the Ohmic dissipation of currents induced by photospheric magneto-convective motions. This drives the magnetic field similar to Parker's field line braiding (or nanoflare) model ([Parker 1972, 1983](#)). The results from this approach successfully reproduced some of the basic properties of the solar corona (e.g. [Gudiksen & Nordlund 2002, 2005b,a](#); [Bingert & Peter 2011, 2013](#)).

The numerical models are able to provide the necessary energy flux in the corona, which is sufficient to heat it to temperatures beyond 1 MK and is consistent with observations ([Bingert & Peter 2011](#)). Furthermore, extreme ultraviolet (EUV) synthetic spectra from these 3D simulations can explain some aspect of the actual observations ([Peter et al. 2004](#); [Warnecke & Peter 2019a](#)). This confirms the validity and efficiency of Parker's field line braiding model to create a hot corona. These models can also be used to study the effects of magnetic helicity injection in the photosphere of active stars on the resulting coronal X-ray emission ([Warnecke & Peter 2019b](#)). This showed that an increase of photospheric magnetic helicity without changing the vertical magnetic field increases the coronal X-ray emission following simple power-law relations. However, the effect of the surface magnetic activity on the coronal X-ray emission in 3D MHD models of solar and stellar coronae has not been studied, yet.

In our study, we focus on the effect of the photospheric magnetic field strength on the coronal X-ray emission. This is motivated by the observation that stars more active than the Sun host stronger surface magnetic field. For that reason, we choose to increase the strength of the vertical surface magnetic field at

the bottom boundary of our computational domain, i.e. we treat the peak (or average) magnetic field strength as a free parameter. All the other parameters remain the same in all numerical experiments. By varying only one parameter (i.e. the surface magnetic field) we can study the exact relation between magnetic flux and coronal emission. Other parameters, important for the coronal energy input, e.g. the photospheric velocity distribution, are observationally ill constraint for other stars and are thus not changed (or varied) in the present work. Our main objective is to relate the synthetic X-ray emission from the numerical models with the surface magnetic flux and relate this to the observed relationships. Furthermore, we will compare our numerical results to our earlier analytical model (Zhuleku et al. 2020) that is briefly summarized in Sect. 2.

2. Analytical scaling relations

The dependence of the coronal X-ray emission to surface magnetic field has been extensively studied for the Sun as well as for other stars (Fisher et al. 1998; Pevtsov et al. 2003; Vidotto et al. 2014; Kochukhov et al. 2020). In Zhuleku et al. (2020) we developed an analytical model to describe the $L_X \propto \Phi^m$ relation, where L_X is the coronal X-ray emission and Φ the total surface unsigned magnetic flux.

Our model is based on the well known Rosner, Tucker & Viana (RTV; Rosner et al. 1978) scaling laws. They derived scalings relating the volumetric heating rate and the loop length to the coronal temperature and pressure. Alternatively, we can express the RTV scaling laws in a way to relate temperature T and number density n with the volumetric heating rate H and loop length L ,

$$T \propto H^{2/7} L^{4/7}, \quad (1)$$

$$n \propto H^{4/7} L^{1/7}. \quad (2)$$

Using these scaling laws together with other relations, we derive an analytical expression for the X-ray emission L_X ,

$$L_X \propto \Phi^m \quad \text{with}$$

$$m = \frac{\beta\gamma}{7} (2\alpha + 8) + \delta \left(\frac{4}{7} + \frac{1}{7}\alpha - \frac{8}{7}\beta\gamma - \frac{2}{7}\alpha\beta\gamma \right). \quad (3)$$

The power law index m depends only on four parameters α , β , γ and δ . The first, α , is related to the temperature sensitivity of the instrument used for the X-ray observations. In general, the X-ray radiation is proportional to the density squared and to a temperature-dependent function $R(T)$. This function $R(T)$ is the sum of all the contribution functions of emission lines and continua, known also as temperature response function, and differs from one instrument to the next. We found that the temperature response function for temperatures below $\log_{10} T[K] = 7$ can be expressed as a power-law (cf. Zhuleku et al. 2020, their Fig.1),

$$R \propto T^\alpha. \quad (4)$$

The parameters β and γ characterize the relation of the energy flux, or the vertical Poynting flux S_z , injected in the corona to the vertical surface magnetic field B and the volumetric heating rate H , again through power-laws,

$$S_z \propto B^\beta \quad (5)$$

$$H \propto S_z^\gamma. \quad (6)$$

The case $\beta = 1$ represents Alfvén wave heating and for $\beta = 2$ nanoflare heating (see also Sect. 6.1). The parameter γ was considered to be unity, $\gamma=1$. Finally, δ relates the surface area covered by a magnetic structure (e.g. a whole active region) to the total magnetic flux,

$$A \propto \Phi^\delta \quad (7)$$

Solar studies have suggested a value of $\delta = 0.819$ (Fisher et al. 1998).

In our analytical study, we found the power-law index m to be in the range from roughly one to almost two (Zhuleku et al. 2020). This result agrees quite well with most observations, but at least one more recent observation finds an even steeper power law connection of $L_X \propto \Phi^m$ with m of 2.68 (Kochukhov et al. 2020).

In the numerical study presented in the following sections, we will assume that the area covered by the magnetic field remains the same, i.e. the change of the surface magnetic flux is solely due to the (average) vertical magnetic field strength. This is equivalent to choose $\delta=0$ in Eq. (7). In this case we get a much steeper power-law in the analytical model, with m up to 4 (Zhuleku et al. 2020, Sect. 5.2, Eq. 15). The numerical study in this paper will give a more detailed comparison to the observations that provide a good match to the observations of Kochukhov et al. (2020).

3. Numerical model setup

3.1. Basic equations

Our model is based on the work of Bingert & Peter (2011, 2013). We use the PENCIL CODE (Brandenburg et al. 2020), where we numerically solve the MHD equations from the photosphere up to the corona. The size of the computational box is $128 \times 128 \times 128$ grid points in Cartesian coordinates (x, y, z) , representing a $50 \times 50 \times 50$ Mm 3 volume with a grid-scale of 390 km in all directions. The comparably small grid size allows us to run a large enough number of numerical experiments to study the relationship between the magnetic activity and coronal emission.

The MHD equations are the continuity, momentum, energy and induction equation connecting density ρ , velocity \mathbf{u} , and temperature T with the magnetic field \mathbf{B} and pressure p :

$$\frac{D \ln \rho}{Dt} + \nabla \cdot \mathbf{u} = 0, \quad (8)$$

$$\frac{D \mathbf{u}}{Dt} = \frac{1}{\rho} \left[-\nabla p + \rho \mathbf{g} + \mathbf{j} \times \mathbf{B} + 2\nu \nabla \circ (\rho \underline{S}) \right], \quad (9)$$

$$\begin{aligned} \frac{D \ln T}{Dt} + (\gamma - 1) \nabla \cdot \mathbf{u} &= \\ &= \frac{1}{c_V \rho T} \left[\eta \mu_0 \mathbf{j}^2 + 2\nu \underline{S}^2 + \nabla \cdot \mathbf{q} + L_{\text{rad}} \right]. \end{aligned} \quad (10)$$

Here the Lagrangian derivative D/Dt is defined as $D/Dt = \partial/\partial t + \mathbf{u} \cdot \nabla$. The current density is given by $\mathbf{j} = \nabla \times \mathbf{B}/\mu_0$. The adiabatic index of an ideal gas is given by $\gamma = 5/3$. We use a constant gravitational acceleration, $\mathbf{g} = (0, 0, -g)$, with $g = 274$ m/s 2 , c_V is the specific heat capacity at constant volume, and $\underline{S} = (u_{i,j} + u_{j,i})/2 - \delta_{ij} \nabla \cdot \mathbf{u}/3$ is the rate of the strain tensor. The resistivity η and viscosity ν are constants through the whole computational box with values $\eta = \nu = 5 \times 10^{10}$ m 2 s $^{-1}$. At the bottom boundary we reduce η to prevent a too large diffusion of the photospheric magnetic field.

The magnetic field is calculated through the vector potential as,

$$\mathbf{B} = \nabla \times (\mathbf{A} + \nabla \phi), \quad (11)$$

which ensure that the $\nabla \cdot \mathbf{B} = 0$ is satisfied at all times. For our simulations we choose the resistive gauge $\phi = \eta \nabla \cdot \mathbf{A}$ so that the induction equation reads,

$$\frac{\partial \mathbf{A}}{\partial t} = \mathbf{u} \times (\nabla \times \mathbf{A}) + \nabla (\eta \nabla \cdot \mathbf{A}). \quad (12)$$

To close the system of equations we need the equation of state for an ideal gas which connects the gas pressure with temperature,

$$p = \frac{k_B}{\mu m_p} \rho T. \quad (13)$$

Where ρ is the mass density, k_B is the Boltzmann constant, μ is the mean atomic weight and m_p is the proton mass.

The radiative losses L_{rad} , are modeled with an optically thin approximation using the radiative loss function $P(T)$. The function $P(T)$ depends on the abundances as well as on the radiation processes that take place like the ionization rate and recombination rate (Meyer 1985; Murphy 1985; Cook et al. 1989). For a detailed discussion in the implementation of the radiative loss function in the code, see Bingert (2009).

The (Spitzer) heat flux along the magnetic field lines \mathbf{q} reads,

$$\mathbf{q} = K_0 T^{5/2} \hat{\mathbf{b}} (\hat{\mathbf{b}} \cdot \nabla T), \quad (14)$$

where $K_0 = 10^{-11} \text{ W}(\text{mK})^{-1}$ (Spitzer 1962) and $\hat{\mathbf{b}}$ is the unit vector of the magnetic field. To speed up the simulations, we replace Eq. 14 by a non-Fourier heat flux scheme. See Warnecke & Bingert (2020) for a detailed description and discussion. Additionally, we use a semi-relativistic correction to the Lorentz force similar to the work of Boris (1970), Gombosi et al. (2002) and Rempel (2017). For details of the implementation, see Chatterjee (2020) and Warnecke & Bingert (2020).

In order to avoid instabilities because of steep gradients in temperature and density, we include in Eq. (10) a (numerical) isotropic heat conduction term and a mass diffusion term (see Bingert 2009). We also include a shock viscosity term for numerical reasons.

3.2. Initial and boundary conditions

The simulations are driven by (horizontal) motions on the solar surface that drive the magnetic field anchored in the photosphere. For the spatial distribution of the vertical magnetic field we employ an observed solar magnetogram (see Fig. 1). This is a snapshot of the active region AR 11102 as observed with the Helioseismic and Magnetic Imager (HMI; Schou et al. 2012) on August 30th, 2010. A detailed description of a similar active region and how it is implemented in the model is discussed in Warnecke & Bingert (2020). These kind of magnetograms represent a typical situation for a solar active region and similar magnetograms have been used as input for data-driven simulations by earlier studies (see e.g. Gudiksen & Nordlund 2005b,a; Bingert & Peter 2011).

For the initial condition, we use a potential field extrapolation to fill the box with magnetic field. The initial temperature

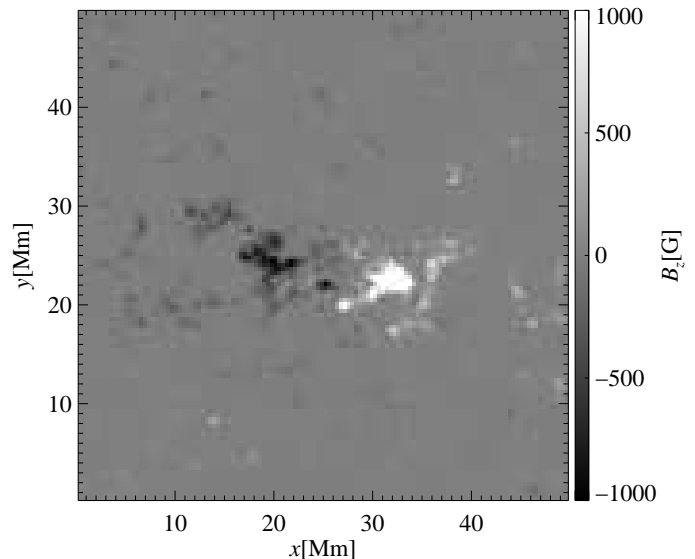


Fig. 1. Initial vertical magnetic field at the bottom boundary of the simulation. This is based on a magnetogram from active region AR 11102 observed with HMI. See Sect. 3.2.

Table 1. Summary of numerical experiments.

Run	$a^{(1)}$	$\Phi [\text{Mx}]^{(2)}$
1B	1	7.4×10^{20}
2B	2	1.5×10^{21}
5B	5	3.7×10^{21}
10B	10	7.4×10^{21}
20B	20	1.5×10^{22}

Notes. ⁽¹⁾ The photospheric magnetic field strength is increased by the factor a . ⁽²⁾ Φ is the total surface unsigned magnetic flux.

stratification follows a vertical profile mimicking the temperature increase into the solar corona. The initial density is calculated from hydrostatic equilibrium and the system is initially at rest with all velocity components set to zero.

In the horizontal x - y plane, all variables are periodic. At the bottom boundary, the temperature T and density ρ have fixed values whereas the horizontal velocities, u_x, u_y have zero vertical gradients. The vertical velocity u_z is set to satisfy the divergence-free condition $\nabla \cdot \mathbf{u} = 0$. We also prescribe a photospheric driver which generates random photospheric velocity motions similar to the solar granular motion. As a result, we shuffle the footpoints of the magnetic loops mimicking the solar photospheric flows similar as in, e.g., Gudiksen & Nordlund (2002, 2005b,a). At the top boundary, all velocities components are zero. To prevent any heat flux going in or out of the computational domain, the gradients of temperature and density are set to zero. The magnetic field is potential both for the bottom and the top boundary.

4. Numerical experiments

4.1. Setup

The main idea of this work is to start with an active region hosting only a small amount of total (unsigned) magnetic flux and then run models with increasing magnetic flux. Our aim is to study how the increase of the photospheric magnetic field

strength contributes to the heating, and thus the X-ray emission of the solar or stellar corona.

We report here on a set of five numerical experiments. The original total unsigned surface magnetic flux of AR11102 is around 7×10^{20} Mx, which is a typical value of a small solar active region. We increase the flux by multiplying the B_z component of the surface magnetic field by a constant ranging from one to twenty (see Table 1). The spatial structure of the magnetic field remains unchanged. In all cases, the total magnetic flux at the bottom boundary is zero, i.e. the surface magnetogram is balanced.

The heating of the coronal loops originates from the dissipation of Poynting flux into heat. More specifically, the conversion of the photospheric magnetic energy to thermal energy is due to the dissipation of the currents created by the random photospheric motions. The stronger the magnetic field, the more Poynting flux reaches the corona, resulting in a higher temperature and X-ray emission.

In our setup, the different total unsigned magnetic fluxes correspond to peak values of the magnetic field ranging from 1 to 20 kG inside the spots. Hence our naming convention in Table 1. The value of 20 kG is very high for a solar active region. Recent observations of solar active regions have measured maximum values of the magnetic field strength on the order of 8 kG (Castellanos Durán et al. 2020). However, this high value was observed only at a very small area on the active region light bridge. Typically the peak magnetic field strengths on solar active regions are on the order of 2 kG to 3 kG. Therefore, of the numerical experiments listed in Table 1, the 5B run can be considered to represent a typical solar active region, with a typical value for the total unsigned flux. Higher values of surface magnetic field could be a common feature, however, of very active stars (Reiners et al. 2014), so the runs 10B and 20B could be considered to be representative of more active stars.

The increase of the surface magnetic field is not the only way to increase the surface magnetic flux. Alternatively we could increase the horizontal extent of an active region while keeping the peak magnetic field strength the same. This will be the main focus of a future study.

4.2. Synthesized emission: X-rays and EUV

Coronal loops are mostly observed in extreme ultraviolet (EUV) wavelengths and X-rays because these wavelengths give access to the million K hot plasma in the corona, and in these wavelengths, the dilute corona is also visible in front of the solar (or stellar) disk that is very bright in the visible range. Therefore, we synthesize the emission in one EUV and one X-ray band. For the EUV band we choose the widely used 171 Å band as seen by the Atmospheric Imaging Assembly (AIA; Lemen et al. 2012) onboard the Solar Dynamic Observatory (SDO; Pesnell et al. 2012). For the X-ray emission, we use the Al-poly filter of the solar X-ray telescope (XRT; Golub et al. 2007) onboard the Hinode observatory (Kosugi et al. 2007).

As mentioned in Sect. 2, the optically thin radiative losses through lines and continua in the corona observed in a given wavelength band are given through

$$\varepsilon = n_e^2 R(T), \quad (15)$$

where n_e is the electron density and $R(T)$ the temperature response (or contribution) function. The response needs to be calculated for each instrument (or filter) by using the effective area depending on wavelength and the spectral lines forming in the

wavelength region covered by the instruments. To calculate $R(T)$ for the 171 Å channel of AIA and the Al-poly filter of XRT, we use the routines in the CHIANTI data base v9 (Dere et al. 1997, 2019) as they are available in the SOLARSOFT package¹. The response functions $R(T)$ for AIA 171 Å and XRT Al-poly are shown in Fig. 3. To calculate the synthetic images as they would be observed by AIA or XRT, ε from Eq. (15) has to be integrated through the computational domain along the chosen line-of-sight. The samples for both channels for the 10B and 20B runs are shown in Fig. 2. These are integrated along the y direction which would correspond to an observation near the limb.

4.3. Horizontal averages

The increase of the surface magnetic field results in an increase in temperature and density in the coronal part of the domain. We calculate the horizontal averages of temperature T , density ρ , and the vertical component of the Poynting flux S_z and then average these in time for an interval of 1 hour. During this time interval the computation reached a relaxed state, i.e. the respective (spatially averaged) quantities show only rather small changes around a mean value (see Sect. 4.4 and Fig. 5). The average vertical stratification of T , ρ and S_z is shown in Fig. 4.

4.3.1. Average Poynting flux deposited in the corona

The photospheric horizontal motions lead to an upward-directed flux of magnetic energy, the Poynting flux. Here we concentrate on its vertical component,

$$S_z = \eta(j \times B)|_z - \frac{1}{\mu_0}(u \times B \times B)|_z \quad (16)$$

that is shown in Fig. 4c for the different runs. In the main part of the computational domain, the $u \times B \times B$ term dominates and (on average) is positive, i.e. upwards directed. The first term including the current, j , is significant only near the bottom where boundary effects of the driving cause high currents. Energetically, this is not relevant, because there the density is high enough that the heating through the currents has virtually no effect.

As we increase the total unsigned magnetic flux from one experiment to the next, the energy stored in the corona increases. The magnetic energy in excess of that of a potential field will be (partly) dissipated and converted into heat. The higher amount of dissipated (free) magnetic energy in the runs with higher magnetic flux leads to higher coronal temperatures and density (see Fig. 4a and Fig. 4b). This is just as expected from the RTV scaling laws (Eqs. 1 and 2) as we will discuss later in Sect. 6.2 (see also Fig. 8).

The Poynting flux of the 1B run at the base of the corona (i.e. at an average temperature of ca. 0.1 MK) barely reaches 50 W/m^2 . Typical estimations based on observations suggest an energy requirement of around 100 W/m^2 for the quiet Sun and 10^4 W/m^2 above active regions (Withbroe & Noyes 1977). Therefore, we cannot expect this run with the lowest magnetic activity to produce a MK corona.

4.3.2. Average temperature and density

All of our simulations self-consistently form a hot upper atmosphere, where the temperature is about two orders of magnitude

¹ <http://www.lmsal.com/solarsoft>

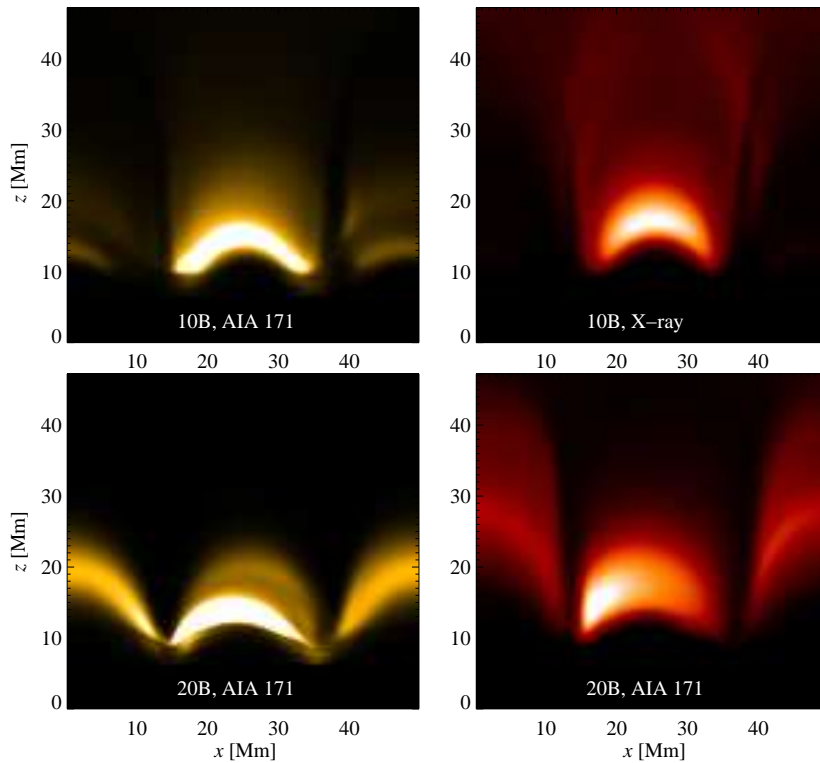


Fig. 2. Side view of the computational domain showing coronal emission. The left two panels show the emission as it would be seen by the 171 Å channel of AIA origination from around 1 MK. The right two panels show X-ray emission as seen by XRT sampling higher temperatures. Here we show snapshots of the two more active models, runs 10B and 20B. The emission here is integrated along the y direction which corresponds to an observation near the limb (of the Sun or a star). The snapshot is taken at time at $t=230$ min, i.e. in the relaxed state. See Sect. 4.2.

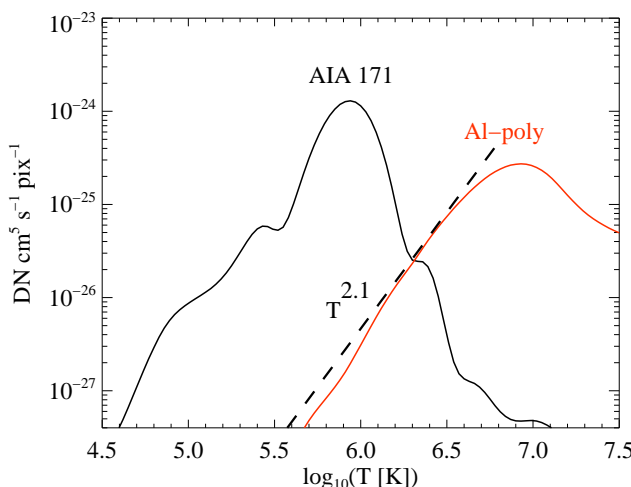


Fig. 3. Temperature response function for the AIA instrument onboard SDO and the XRT onboard Hinode. The Black line shows the 171 Å channel of the AIA, the red line shows the Al-poly filter of the XRT. Just for illustration, the dashed black line indicates a power-law approximation to XRT at temperatures below 10^7 K. See Sect. 4.2.

higher than at the surface (cf. Fig. 4a). A higher total unsigned flux in the photosphere (cases 1B through 20B) corresponds not only to higher Poynting fluxes, but also to higher temperatures and density. The values shown in Fig. 4a and b are averages only, so the peak values are significantly higher, up to 5 MK and more.

The experiment with the least magnetic activity (run 1B) fails to create a million-Kelvin hot corona, as expected. Still, we consider it in the analysis of the power-law relation in Sect. 5. The main focus of this work is to relate the coronal emission to the surface magnetic activity through a number of numerical experiments,

and in this sense also a model that is not active enough to produce a MK corona gives valuable insight.

Besides the increased temperature and density, the models with higher magnetic activity also have the transition region located at lower heights. From this, it is clear that the height where the average temperature reaches 0.1 MK is lower for the runs with more magnetic flux. The higher energy input leads to a higher heat flux back to the Sun. Because the radiation is most efficient at lower temperatures (at 0.1 MK and below), in equilibrium the transition region will be found at lower temperatures and thus higher densities where it can radiate the energy. The consequence is that the density (and the pressure) throughout the corona will be higher, just as seen in our simulations.

The average density profile ρ displays similar (qualitative) behavior as the temperature. In the coronal part the density is high for the runs with higher magnetic flux (Fig. 4b). Following a steep drop over many orders of magnitude in the low atmosphere, the density remains almost constant in the coronal part. This is simply because of the large barometric (pressure) scale height at high temperatures. At 1 MK this scale height is about 50 Mm and thus comparable to the vertical extent of our computational domain, hence the horizontally averaged pressure and density are roughly constant in the coronal part of our box.

4.4. Temporal evolution

The quantities we consider in our model vary significantly with time, especially during the early phase of the simulations. To investigate the average behavior of our model, we have to consider a time frame of the numerical model where the system reached a relaxed (or evolved) state. During that state, the quantities show (comparably small) variations around an average value.

To illustrate this, we first consider the total heating in the coronal part of the computational domain. We define the coronal part as the volume above the height where the horizontally av-

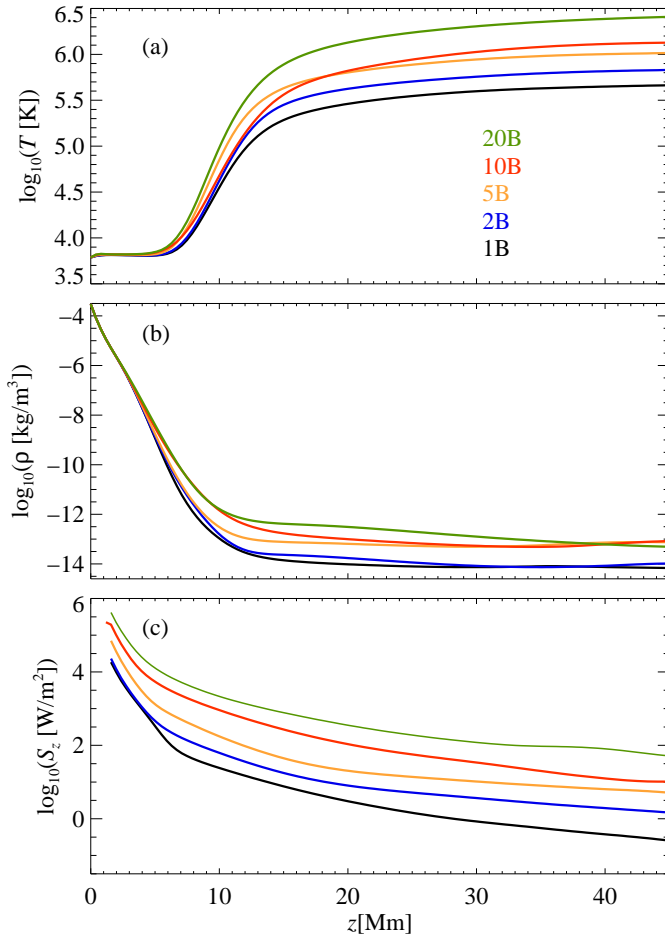


Fig. 4. Horizontal averaged quantities as a function of height. We show temperature T (panel a), density ρ (panel b), and the vertical component of the Poynting flux S_z (panel c). The colors represent the different runs as indicated in the legend (cf. Table 1). The quantities are averaged horizontally for each snapshot and then in time for 1 hour (from times 3.5 hr to 4.5 hr as indicated in Fig. 5 by the vertical dashed lines. For the Poynting flux we omitted the first 3 grid points that show boundary effects. See Sect. 4.3.

eraged temperature is 10^5 K. Because the temperature gradient in the transition region around 10^5 K is rather steep, the exact choice of this temperature does not matter. So we define the total coronal heating H_{tot} as the volume integral over this coronal part, here symbolized by the subscript cor,

$$H_{\text{tot}} = \int_{\text{cor}} \eta \mu_0 j^2 dV. \quad (17)$$

The temporal variation of the heating is shown in Fig. 5 for the five models with different magnetic activity. We see a clear ordering of the heating with the surface magnetic flux (increasing for run 1B through 20B), which we will discuss in more detail later in Fig. 7 and Sect. 6.1. In terms of the temporal evolution, we find that the heat input reaches a relaxed state rather quickly, probably within less than an hour. This is expected, because the stresses applied on the magnetic field in the photosphere will propagate with the Alfvén speed. The corresponding Alfvén crossing time for perturbations to cross the whole box is on the order of minutes.

The situation for the relaxation time is different when considering the coronal emission in X-rays and EUV. Here it turns out

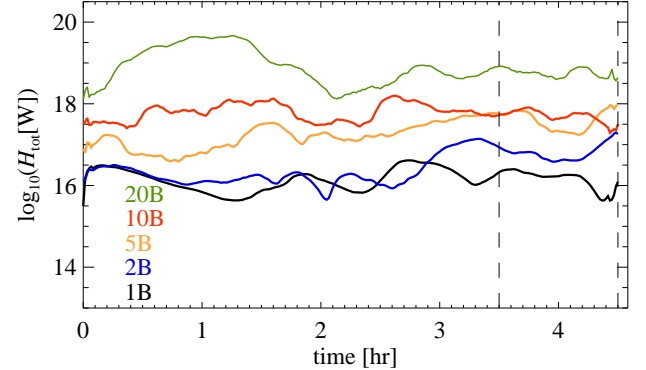


Fig. 5. Total coronal heating H_{tot} as a function of time. The vertical dashed lines indicate the time span used for the temporal averages. The colors represent the different runs as indicated in the legend (cf. Table 1). See Sec. 4.4.

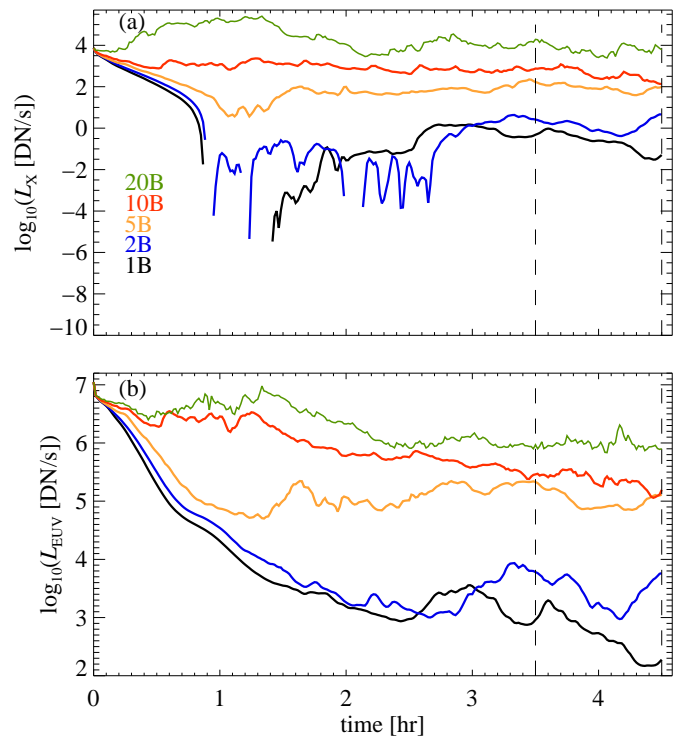


Fig. 6. Temporal evolution of the coronal emission from integrated over the whole computational domain. Panel (a) shows the X-ray emission as seen by XRT in the Al-poly filter, panel (b) the EUV emission as it would be seen by AIA in the 171 Å channel. The vertical dashed lines indicate the time span used for time averaging. The colors represent the different runs as indicated in the legend (cf. Table 1). See Sec. 4.4.

that we have to wait for about 3 hours before the models reach a relaxed state. Mainly, this is because of the radiative cooling time under typical coronal conditions which is on the order of 1 hour (Aschwanden 2005). Therefore we will examine the temporal evolution of the coronal radiation in some more detail.

We now turn to the variability of the X-ray and EUV emission (see Fig. 6). Because the lower cool part of the atmosphere does not produce any significant amount of X-rays or EUV, we simply integrate the coronal emission over the whole computational domain. This is equivalent to the luminosity originating from the domain, L_X and L_{EUV} . Because we use the temperature response functions for XRT and AIA (Sect. 4.2, Fig. 3), we get

the counts per second as expected for the respective instrument from the whole loop in the box (cf. Fig. 2). For the comparison between the different model runs it is important that we use the same scale for the different models. Based on this, we see a clear scaling of the coronal emission with magnetic activity, in a similar way as we see it for the heat input. We will discuss this in more detail in Fig. 9 and Sect. 6.3.

Mostly, the coronal emission shows an initial drop on the timescale of almost an hour, in particular for EUV channel of AIA 171 Å in the runs with low magnetic activity. This is because the atmosphere of the initial condition is rather hot, and the plasma is cooling down until it reaches a new equilibrium after a few coronal radiative cooling times (Fig. 6). Here we see that all model runs reach a relaxed state after about 2.5 to 3 hours. With some safety margin we can thus assume that from 3.5 to 4.5 hours the models have reached a relaxed state (see vertical dashed lines in Figs. 5 and 6). All the time averages discussed in our study are taken over this time frame.

5. Scaling relations in numerical experiments

To characterize the model runs with different magnetic activity, i.e. unsigned magnetic surface flux, we investigate the scaling relations in the form of power laws between different parameters. In Sect. 4 we showed that the enhancement of the photospheric magnetic flux lead to a substantial increase of temperature, density, Poynting flux and coronal emission. In this section, we discuss the power-law relations of various quantities averaged in space and time quantities. We will discuss these results in Sect. 6 including the study of Zhuleku et al. (2020).

We first concentrate the relation of the the vertical component of the average Poynting flux $\langle S_z \rangle$ to the unsigned surface magnetic flux Φ and the averaged total coronal heating $\langle H_{\text{tot}} \rangle$ (see Fig. 7). Each cross in the two figures represent averaged values of the respective quantities in each individual numerical model (cf. Table 1). Here we take the the horizontal average of the Poynting flux $\langle S_z \rangle$ at the height where the horizontally averaged temperature is 10^5 K, i.e. the base of the corona and average it in time from 3.5 to 4.5 hr (see Sect. 4.4). This represents the energy flux (per unit area) into the corona. The total averaged coronal volumetric heating $\langle H_{\text{tot}} \rangle$ is calculated according to Eq. (17) and then averaged between times 3.5 and 4.5 hr as discussed in Sect. 4.4. The unsigned surface flux Φ is the integral over the bottom boundary, i.e. the stellar surface which is constant in time. The bars in Fig. 7 indicate the standard deviation of the respective quantity in time. For relations displayed in Fig. 7 we perform power-law fits (indicated by the red line) that result in

$$\langle S_z \rangle \propto \Phi^\beta \quad \text{with} \quad \beta = 1.71 \pm 0.42, \quad (18)$$

$$\langle S_z \rangle \propto \langle H_{\text{tot}} \rangle^\Gamma \quad \text{with} \quad \Gamma = 0.88 \pm 0.22. \quad (19)$$

Here Γ corresponds to $1/\gamma$ from the analytical model in Eq. (6) and Zhuleku et al. (2020). The two scalings (18) and (19) imply that the heating increases roughly quadratically with magnetic flux, $\langle H_{\text{tot}} \rangle \propto \Phi^{1.94}$.

As a next step, we relate the coronal temperature T and density ρ to the total coronal heating $\langle H_{\text{tot}} \rangle$. Here we test to what extent the coronal temperature and density in our numerical model deviates from the analytic RTV scaling laws as given in Eqs. (1) and (2). For this, we calculate the average temperature $\langle T \rangle$ and density $\langle \rho \rangle$ in the corona in a height range from $z=10$ Mm to 20 Mm for each of the models. We choose this particular height range because here the bright structures appear (see Fig. 2). If we

would also include higher regions of the box, the averages would no longer represent the actually visible parts of the corona. In addition, we average $\langle T \rangle$ and $\langle \rho \rangle$ in time from 3.5 to 4.5 hr as discussed in Sect. 4.4. We show the corresponding plots including the power-law fits of $\langle T \rangle$ and $\langle \rho \rangle$ as a function of the total coronal heating H_{tot} in Fig. 8. The power-law fits yield

$$\langle T \rangle \propto \langle H_{\text{tot}} \rangle^a \quad \text{with} \quad a = 0.24 \pm 0.03, \quad (20)$$

$$\langle \rho \rangle \propto \langle H_{\text{tot}} \rangle^b \quad \text{with} \quad b = 0.76 \pm 0.05. \quad (21)$$

Finally, we address the relation of the X-ray emission to the heating rate and the unsigned surface magnetic flux. As the photospheric magnetic flux is larger for models with higher magnetic activity, also the total dissipated energy is larger. And because the X-ray emission is expected to increase with the heating rate, it should also be larger for higher unsigned magnetic flux. For the analysis we consider the averaged emission, $\langle L_X \rangle$, that is integrated over whole computational domain and averaged as the other quantities from 3.5 to 4.5 hr. The corresponding relations are plotted in Fig. 9 and Fig. 10a, and the power-law fits give

$$\langle L_X \rangle \propto \Phi^m \quad \text{with} \quad m = 3.44 \pm 0.28, \quad (22)$$

$$\langle L_X \rangle \propto \langle H_{\text{tot}} \rangle^q \quad \text{with} \quad q = 1.78 \pm 0.15. \quad (23)$$

We apply the same integration and time averaging to the EUV emission as seen by AIA in its 171 Å channel. Its relation to the heat input is displayed in Fig. 10b and the power-law fit reveals an almost linear relation,

$$\langle L_{\text{EUV}} \rangle \propto \langle H_{\text{tot}} \rangle^p \quad \text{with} \quad p = 1.05 \pm 0.09. \quad (24)$$

6. Discussion

6.1. Energy input into the corona

The solar coronal heating problem and the underlying physical mechanism has been extensively discussed the last 70 years. Two of the main mechanisms that are being considered are the Alfvén-wave model (e.g. van Ballegooijen et al. 2011) and the field-line braiding or nanoflare model (Parker 1972, 1983). These two processes have a different dependence of the Poynting flux, and hence the heat input, on the magnetic field. A simple estimate for these dependencies has been given by Fisher et al. (1998). Here we follow their arguments. For an Alfvén wave with constant amplitude, the Poynting flux will be proportional to the propagation speed, i.e. the Alfvén velocity, and hence to the magnetic field B , $S_z \propto B$. For the field-line braiding, the Poynting flux will be set by the driving motions with speed u and the magnetic field, $S \propto u \times B \times B$, and hence the scaling would be $S_z \propto B^2$ (assuming that the driving motions do not change with B).

In our numerical experiments we find a power-law scaling between Poynting flux and (unsigned) magnetic flux with a power-law index of about 1.7 ± 0.4 , see Eq. (18) and Fig. 7a. Within the uncertainties this is consistent with the above (analytical) estimate of 2. Of course, this is not surprising, because our in our model we drive the coronal magnetic field through foot-point motions consistent with the field-line braiding scenario. Still, it is reassuring to recover this scaling by our numerical model.

Observationally it is clear that Alfvén waves are present in the corona (e.g. Tomczyk et al. 2007). Still, it remains unclear if the energy they carry would be sufficient to energize the corona. Waves might play a role in the quiet Sun corona, but they seem

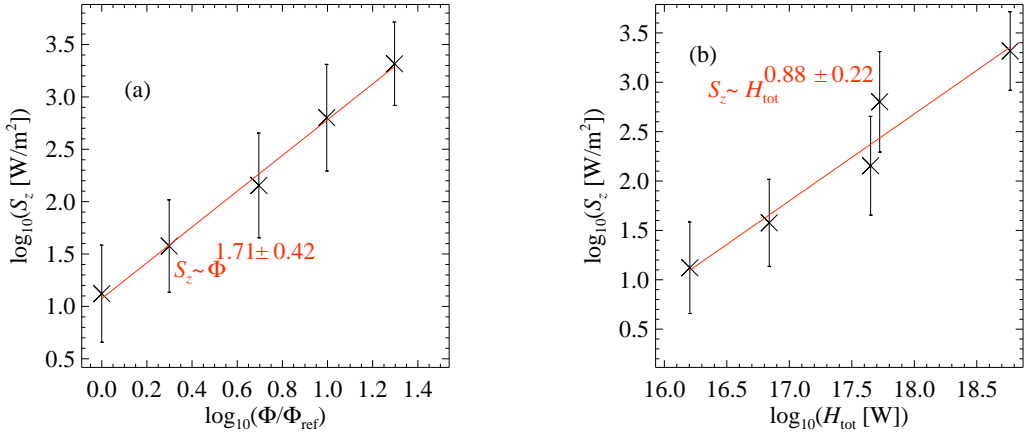


Fig. 7. Scaling of average Poynting flux $\langle S_z \rangle$ with unsigned surface flux Φ and average coronal heating $\langle H_{\text{tot}} \rangle$. Each data point represents an average for one of the model runs with different unsigned surface magnetic flux as listed in Table 1. As a reference for the magnetic flux, Φ_{ref} , we choose the magnetic flux of the least active setup, run 1B (cf. Table 1). The bars represent the standard deviation of S_z in time. The red lines are power-law fits to the data. See Sects. 5 and 6.1.

to not be able to heat active regions (McIntosh et al. 2011). Our particular model can contribute little to this discussion, because we do not fully resolve Alfvén waves, which is because of the comparably large dissipation.

Finally, we expect that the total energy dissipated in the coronal volume matches the Poynting flux at the base of the corona. In this case the Poynting flux should scale linearly with the total amount of energy dissipated in the corona. In our numerical experiments we find a power-law relation with a power-law index of about 0.9 ± 0.2 , which is consistent with linear, see Eq. (19) and Fig. 7b.

6.2. RTV scaling laws compared to numerical experiments

One obvious check for the numerical experiments is to what extent the averaged quantities will follow the RTV scaling laws Eqs. (1) and (2). Of course, because of the spatial and temporal variability we cannot expect a perfect match, but the average quantities should roughly follow these scalings, as it was found in an earlier model for one single (small) solar active region (Bourdin et al. 2016).

The original RTV scalings in Eqs. (1) and (2) include a dependence on the loop length L . In our numerical models, however, the physical size of the computational box is kept constant. Therefore, the coronal loops can be considered to have similar lengths. Consequently, in this study we only have to consider the dependence of temperature and density on (total) heating in the coronal volume, H_{tot} .

For a comparison to the RTV scalings one should not only compare the power-law indices of the scaling, but also the absolute values of the temperature T and density ρ as given in the original paper by Rosner et al. (1978). To calculate the predictions from the RTV scalings, i.e. T_{RTV} and ρ_{RTV} , we use a loop length of $L=30$ Mm, which is similar to the average loop length we find in the emission patterns synthesized from the model (see Fig. 2). For the volumetric heating rate we use the (total) heating in the coronal volume, $\langle H_{\text{tot}} \rangle$, divided by the coronal volume, which gives the (average) volumetric heating. The resulting variation of T_{RTV} and ρ_{RTV} with $\langle H_{\text{tot}} \rangle$ is shown in Fig. 8 (blue lines). Obviously, the power law-indices of 0.29 and 0.57 for these correspond to 2/7 and 4/7 in Eqs. (1) and (2).

The power-law relation of the average temperatures $\langle T \rangle$ and density $\langle \rho \rangle$ in the numerical models with $\langle H_{\text{tot}} \rangle$ are close to what is expected from RTV. However, both the temperature and the density are significantly lower, by about a factor 2 and 3, see Fig. 8 and Eqs. (20) and (21).

The reason for this underestimation is mainly due to the averaging process of the temperature and density. The bright loops are hotter and denser than the ambient corona so that the averages underestimate the values corresponding to the RTV scaling relations. Still, we conclude that the numerical models and the analytical scaling relations are consistent (as an order-of-magnitude estimation).

6.3. Relation of X-ray emission to surface magnetic flux

The central result of our study is the power-law relation between the synthetic X-ray emission L_X and the unsigned surface magnetic flux Φ . We show this relation $L_X \propto \Phi^m$ with a power-law index m of about 3.4 ± 0.3 in Fig. 9, see also Eq. (22).

This L_X vs. Φ^m relationship has been extensively discussed in numerous observational studies of the Sun and of stars of different spectral types (see e.g. Fisher et al. 1998; Pevtsov et al. 2003; Vidotto et al. 2014). However, the physical reasons behind the observed power-law relation remained unclear. Observations of various solar features and solar-like stars suggest a relation close to but slightly steeper than linear, i.e. $m \gtrsim 1$ (e.g. Fisher et al. 1998; Pevtsov et al. 2003). More recent studies find the power-law to be close to quadratic ($m=1.8$; Vidotto et al. 2014) or even steeper ($m=2.68$; Kochukhov et al. 2020). While Kochukhov et al. (2020) considered stars similar to the Sun in terms of spectral type, all these were considerably more active than the Sun in terms of X-ray luminosity. The large sample of Vidotto et al. (2014) also contained mainly stars being significantly more active than the Sun.

An almost linear relation of L_X vs. Φ could be simply understood by increasing the number of active regions on a (solar-like) star. If the filling factor of active regions is low and one simply doubles the number of active regions, both the total unsigned magnetic flux on the stellar surface and the X-ray emission would double. Hence the linear relation between L_X and Φ . This, in principle, could explain the findings of Fisher et al. (1998) and Pevtsov et al. (2003).

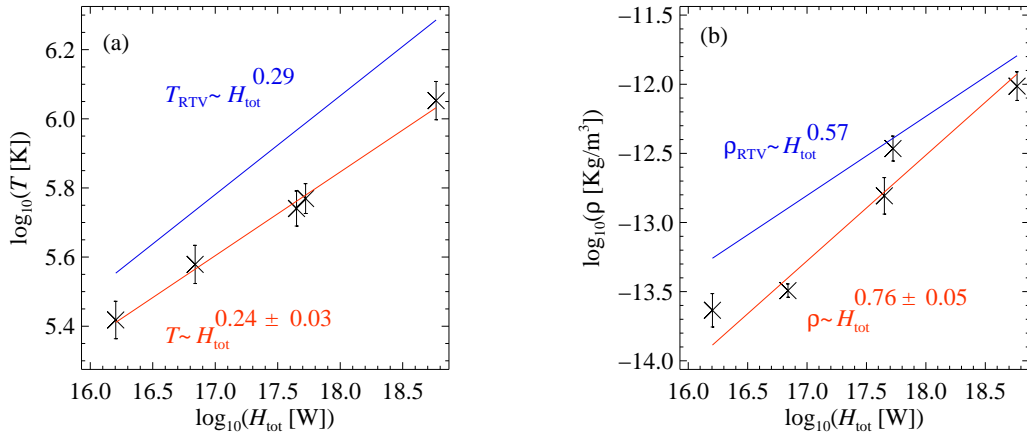


Fig. 8. Scaling of average temperature $\langle T \rangle$ and density $\langle \rho \rangle$ with average coronal heat input $\langle H_{\text{tot}} \rangle$. Each data point represents an average for one of the model runs with different unsigned surface magnetic flux listed in Table 1. The bars represent the standard deviation of the spatial averages of T and ρ in time. The red lines are power-law fits to the data. The blue lines indicate what is expected from the RTV scaling laws. See Sects. 5 and 6.2.

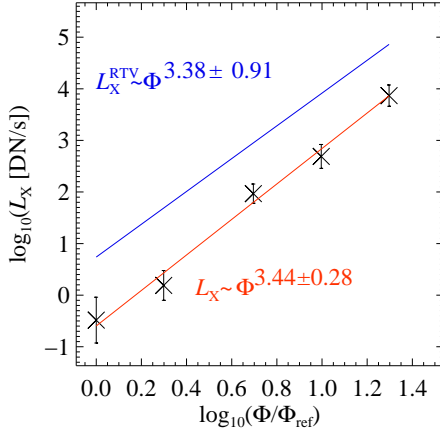


Fig. 9. Scaling of average X-ray emission $\langle L_X \rangle$ with unsigned surface flux Φ . Each data point represents an average for one of the model runs with different unsigned surface magnetic flux listed in Table 1. As a reference for the magnetic flux, Φ_{ref} , we choose the magnetic flux of the least active setup, run 1B (cf. Table 1). The bars represent the standard deviation of L_X in time. The red lines are power-law fits to the data. The blue lines show the analytic power-law relations based on the RTV scaling laws. See Sects. 5, 6.3 and 6.4.

Active stars show X-ray luminosities (compared to their bolometric luminosity) that can be three or more orders of magnitude larger than that of the Sun (e.g. Vidotto et al. 2014). In this case there would be simply not enough space on the star to cover it with enough (solar-like) active regions. This means, the X-ray emission per active region has to increase. This is exactly what we find in our model when increasing the magnetic flux of an active region while keeping its size (i.e. area) the same. This leads to a steep increase of X-ray luminosity with surface magnetic flux, an increase that is even steeper than observed: the power-law index m for $L_X \propto \Phi^m$ is about 3.4 in our model, while the largest value found in observations is below 2.7 (Kochukhov et al. 2020). This overestimation of the power-law index by our model indicates that on real stars we might find a mixture of an increase of the numbers of active regions that goes together with the increase of the peak magnetic field strength (or magnetic flux per active region) for more active stars.

6.4. Analytical model for scaling of X-ray emission

We will now compare the scaling of $L_X \propto \Phi^m$ to some basic analytical considerations. In an earlier study we derived an analytical scaling of the X-ray emission with surface magnetic flux that is based on the RTV scaling relations (Zhuleku et al. 2020). As discussed in the summary of that model in Sect. 2, there we used a scaling of active region size with (unsigned) magnetic flux based on solar observations, see Eq. (7). In contrast, in our numerical model we keep the size or area covered by the active region constant, hence here the power-law index in Eq. (7) is $\delta=0$. This simplifies our analytical scaling from Eq. (3) to

$$m = \frac{\beta\gamma}{7}(2\alpha + 8). \quad (25)$$

According to Eq. (4), α is the power-law-index relating the temperature response (or contribution) function to temperature. Here we approximate this for X-rays as seen by the XRT on Hinode (see Fig. 3), where a power-law fit yields

$$R_X \propto T^\alpha \quad \text{with} \quad \alpha = 2.1 \pm 0.2. \quad (26)$$

We give a more extensive discussion on the temperature responses for different instruments in Zhuleku et al. (2020).

The other two parameters β and γ in Eq. (25) we take from the relations of the Poynting flux to the unsigned surface magnetic flux and the total heating in Eqs. (18) and (19), with $\gamma=1/\Gamma$ in Eq. (19). This results in the analytic scaling (based on RTV) of

$$L_X^{\text{RTV}} \propto \Phi^{m'} \quad \text{with} \quad m' = 3.38 \pm 0.91. \quad (27)$$

This is overplotted onto the results from the numerical experiments in Fig. 9 as a blue line. We conclude that this power-law index is in good agreement with the value we obtained from the numerical models, see Eq. (22) and Fig. 9.

Just as for the comparison to the RTV scalings in Sect. 6.2, also here it is not sufficient to find a match of the power law index, but also the absolute values of the derived X-ray emission have to be of the same order for a good match. To get the constant of proportionality in Eq. (27), we have to assign a volume of the emitting structure described in the analytical scaling. For the comparison to our numerical model we thus assign the volume of the loop(s) dominating the coronal emission. Using the loops

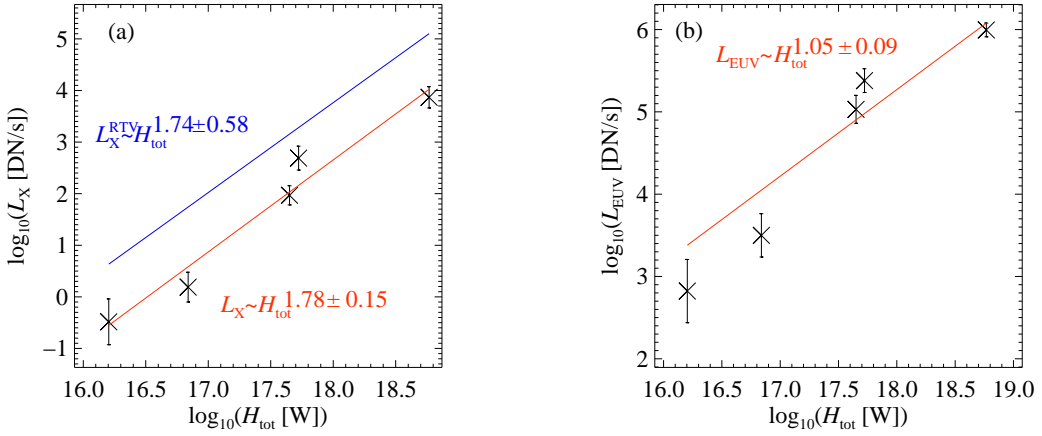


Fig. 10. Scaling of average X-ray and EUV emission, $\langle L_X \rangle$ and $\langle L_{\text{EUV}} \rangle$ with average coronal heating $\langle H_{\text{tot}} \rangle$ for model runs listed in Table 1. The bars represent the standard deviation of L_X and L_{EUV} in time. The red lines are power-law fits to the data. The blue line in panel (a) indicates what is expected from the RTV scaling laws. See Sects. 5 and 6.5.

in Fig. 2 as a guideline, these have a length and a radius of about $L \approx 30 \text{ Mm}$ and $r \approx 2.5 \text{ Mm}$. With the volume of $V = \pi R^2 L$ we then find the total X-ray radiation from the loops based on the (RTV) scaling relations of L_X^{RTV} . Within an order of magnitude these match what we find in the numerical study. The deviation is mainly because of the factor of about 3 difference in density (cf Sect. 6.2) which enters the emission quadratically.

6.5. X-ray and EUV emission versus coronal energy input

Common sense suggests that a higher energy input into the corona should result in a higher X-ray emission. Indeed, this is what we find in Fig. 10a. However, we find an almost quadratic relationship, $\langle L_X \rangle \propto \langle H_{\text{tot}} \rangle^{1.8}$, cf. Eq. (24). This non-linearity is counter-intuitive: Assuming that the plasma in our numerical model has reached a relaxed state, then whatever energy reaches the corona should be radiated away as X-ray emission (i.e., naively, we would expect a linear dependence).

This (roughly) quadratic relation can be understood when going back to the RTV scalings. The X-ray emission is given by $L_X \propto n^2 R_X$. Combining this with the fit to the X-ray response function in Eq. (26) and the RTV scaling relations Eqs. (1) and (2) provides the analytical scaling for the X-ray emission with (average) coronal heat input,

$$L_X^{\text{RTV}} \propto \langle H_{\text{tot}} \rangle^{q'} \quad \text{with} \quad q' = 1.74 \pm 0.58. \quad (28)$$

This is shown in comparison to the results from the numerical model in Fig. 10a as a blue line. As before, we assumed a constant loop length, because the active region size is the same for all the numerical experiments.

This consideration provides an understanding of the non-linear relation between X-ray output and heat input. In the corona the energy input will be only partly balanced by the X-ray output (also heat conduction, a wind outflow and radiation at other wavelengths will play a role). Because the X-ray output shows a non-linear temperature dependence, naturally, it will also be connected in a non-linear fashion to the heat input. The simple RTV scaling relations, together with the temperature response of X-ray emission, give rise to the roughly quadratic dependence of X-rays on heat input.

The situation changes when investigating another wavelength region, which essentially implies to probe a different temperature range. For this we use the channel as seen by AIA at

171 Å. The EUV emission in this band is mostly originating from temperatures around 1 MK (cf. Fig. 3). If we apply the same analysis as for the X-ray emission, the numerical experiments show an almost linear scaling with heat input, $\langle L_{\text{EUV}} \rangle \propto \langle H_{\text{tot}} \rangle^{1.1}$, see Fig. 10b. The reason this relation is less steep than for the X-rays is because of the different temperature response in the EUV.

The response in the EUV cannot be simply approximated by a power law (see Fig. 3). However, over the temperature range of most our models, as a very rough zeroth order approximation we could assume the response in the EUV channel to be constant. This would be consistent with the power-law index for the response function, i.e. α in Eq. (4), to be zero. Following the above procedure for the X-rays, in analogy to Eq. (28) we would find $L_{\text{EUV}}^{\text{RTV}} \propto \langle H_{\text{tot}} \rangle^{1.14}$ for the EUV emission. This result compares well with the numerical experiments (cf. Fig. 10b), but certainly it has to be taken cum grano salis, which is because of our very rough assumption of $\alpha=0$. This is why we do not overplot an analytical approximation in Fig. 10b as we did for the other scaling relations. Still, this consideration underlines the importance of the temperature response for establishing a relationship between coronal emission and heat input.

6.6. Relating the X-rays the EUV emission

Finally, we briefly investigate the scaling relation between the X-ray and the EUV emission. Solar and stellar studies have addressed the relation between the radiative fluxes in different wavelength bands, also called flux-flux-relations. One prominent example is the relation between the coronal X-ray radiative flux and the radiance in the chromospheric Ca II line with $F_X \propto (F_{\text{CaII}})^{1.67}$ (e.g. Schrijver 1983). Power-law relations have also been derived with other chromospheric and transition region lines, e.g. Mg II, Si II, C II, and C IV (Schrijver 1987). The higher the temperature in the source region of the emission, the steeper the power-law relation of the respective line to the surface magnetic field (e.g. Testa et al. 2015). This implies that the relation of $\langle L_X \rangle$ vs. $\langle L_{\text{EUV}} \rangle$ is less steep than the relation of X-rays to Ca II.

In the numerical models we find that the relation between X-rays and the 1 MK EUV emission follows a power law with about $\langle L_X \rangle \propto \langle L_{\text{EUV}} \rangle^{1.3}$, see Fig. 11. This is also consistent with other numerical studies (see e.g. Warnecke & Peter 2019b, their

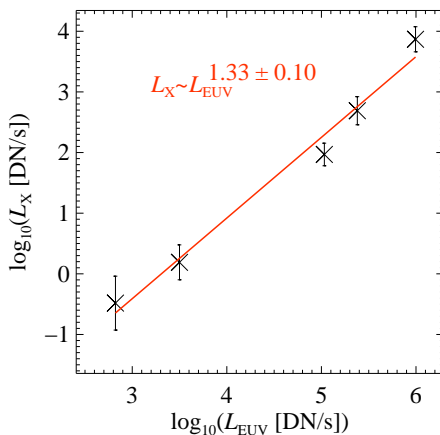


Fig. 11. Scaling of averages of X-ray emission $\langle L_X \rangle$ with EUV emission $\langle L_{\text{EUV}} \rangle$ for model runs listed in Table 1. The bars represent the standard deviation of L_X in time. The red line is a power-law fit to the data. See Sect. 6.6

Fig. 10b). So indeed, as expected, it is less steep than X-rays to Ca II with a power-law index about 1.7.

Our numerical models are not realistic enough when it comes to the cooler parts of the atmosphere, in the transition region around 10^5 K and the in particular in the cooler chromosphere. Still we see the right trend for the flux-flux relations and it will be left for future more realistic models to fully explore the flux-flux relations.

7. Conclusions

We performed a series of 3D MHD numerical simulations of active regions. With this we address the question how the (X-ray) emission from stellar coronae scales with the surface magnetic flux. Observationally this power-law scaling $L_X \propto \Phi^m$ is well established with the most recent studies giving power-law indices m in the range of below 2 to almost 3. (Vidotto et al. 2014; Kochukhov et al. 2020). So far, the physical basis for this relation is poorly understood in terms of (numerical) models.

For our model series we assumed that the area covered by the active region remains the same, and we changed the peak (or average) vertical field strength B to change the (unsigned) magnetic flux at the surface by a factor of 20. This resulted in a change of the X-ray emission by more than four orders of magnitude. The scaling we found in our numerical experiments is a power law with an index $m \approx 3.4$, i.e. a bit steeper than found in observations. As we discussed in Sect. 6.3, this difference can be understood if on the real star there are not only active regions with higher magnetic flux (but the same area), but if there is also a larger filling factor of active regions, or in other words a larger number of active regions.

The results of our numerical experiments are consistent with an analytical scaling model (Zhuleku et al. 2020). This is based on the RTV scaling laws connecting the temperature and density to the heating rate and size of the coronal structure and the temperature response of the wavelength band the observations are performed. With this we have a clear understanding how and why the radiative X-ray output changes in a non-linear fashion in response to the heat input, and hence the surface magnetic flux.

In our numerical model we choose the specific approach to increase the surface magnetic flux by increasing the field strength. This is motivated by the very high field strengths seen

on active M dwarfs of up to 8 kG on average (e.g. Reiners 2012). The average being so large suggests that the highest field strengths on these stars could be even higher, maybe consistent with our model. Still, to investigate further possibilities we will study the response of the coronal emission to an increase of the magnetic flux by increasing the area of the active region(s) in a future project.

Of course our models for individual active regions cannot be expected to fully account for all aspects of the scaling of coronal emission with (unsigned) surface magnetic flux. Still, our approach indicates a way to understand the excessive increase of the observed X-ray emission by 4 orders of magnitude from solar-type activity to fast rotating active stars (by e.g. Pizzolato et al. 2003; Vidotto et al. 2014).

Acknowledgements. The simulations have been carried out at GWDG in Göttingen and the Max Planck Computing and Data Facility (MPCDF) in Garching. This work was supported by the International Max Planck Research School (IMPRS) for Solar System Science at the University of Göttingen. J.W. acknowledges funding by the Max-Planck-Princeton Center for Fusion and Astro Plasma Physics. This project has received funding from the European Research Council (ERC) under the European Union’s Horizon 2020 research and innovation programme (grant agreement n.o 818665 “UniSDyn”).

References

Aschwanden, M. J. 2005, Physics of the Solar Corona. An Introduction with Problems and Solutions (2nd edition) (Springer-Verlag Berlin Heidelberg New York)

Bingert, S. 2009, Heating of the corona in a 3D MHD forward model approach (Univ. Freiburg (Breisgau)), <http://dx.doi.org/10.23689/fidgeo-19>

Bingert, S. & Peter, H. 2011, A&A, 530, A112

Bingert, S. & Peter, H. 2013, A&A, 550, A30

Boris, J. P. 1970, In A Physically Motivated Solution of the Alfvén Problem:NRL memorandum report

Bourdin, P.-A., Bingert, S., & Peter, H. 2016, A&A, 589, A86

Brandenburg, A., Johansen, A., Bourdin, P. A., et al. 2020, arXiv e-prints, arXiv:2009.08231

Castellanos Durán, J. S., Lagg, A., Solanki, S. K., & van Noort, M. 2020, ApJ, 895, 129

Chatterjee, P. 2020, Geophysical and Astrophysical Fluid Dynamics, 114, 213

Cook, J. W., Cheng, C.-C., Jacobs, V. L., & Antiochos, S. K. 1989, ApJ, 338, 1176

Dere, K. P., Del Zanna, G., Young, P. R., Landi, E., & Sutherland, R. S. 2019, ApJS, 241, 22

Dere, K. P., Landi, E., Mason, H. E., Monsignori Fossi, B. C., & Young, P. R. 1997, A&AS, 125, 149

Fisher, G. H., Longcope, D. W., Metcalf, T. R., & Pevtsov, A. A. 1998, ApJ, 508, 885

Golub, L., Deluca, E., Austin, G., et al. 2007, Sol. Phys., 243, 63

Gombosi, T., Tóth, G., Zeeuw, D., et al. 2002, Journal of Computational Physics, 177, 176

Gudiksen, B. V. & Nordlund, Å. 2002, ApJ, 572, L113

Gudiksen, B. V. & Nordlund, Å. 2005a, ApJ, 618, 1031

Gudiksen, B. V. & Nordlund, Å. 2005b, ApJ, 618, 1020

Kochukhov, O., Hackman, T., Lehtinen, J. J., & Wehrhahn, A. 2020, A&A, 635, A142

Kosugi, T., Matsuzaki, K., Sakao, T., et al. 2007, Sol. Phys., 243, 3

Lemen, J. R., Title, A. M., Akin, D. J., et al. 2012, Sol. Phys., 275, 17

McIntosh, S. W., de Pontieu, B., Carlsson, M., et al. 2011, Nature, 475, 477

Meyer, J. P. 1985, ApJS, 57, 173

Murphy, R. J. 1985, PhD thesis, University of Maryland

Parker, E. N. 1972, ApJ, 174, 499

Parker, E. N. 1983, ApJ, 264, 642

Pesnell, W. D., Thompson, B. J., & Chamberlin, P. C. 2012, Sol. Phys., 275, 3

Peter, H., Gudiksen, B. V., & Nordlund, Å. 2004, ApJ, 617, L85

Pevtsov, A. A., Fisher, G. H., Acton, L. W., et al. 2003, ApJ, 598, 1387

Pizzolato, N., Maggio, A., Micela, G., Sciortino, S., & Ventura, P. 2003, A&A, 397, 147

Reiners, A. 2012, Living Reviews in Solar Physics, 9, 1

Reiners, A., Schüssler, M., & Passegger, V. M. 2014, ApJ, 794, 144

Rempel, M. 2017, ApJ, 834, 10

Rosner, R., Tucker, W. H., & Vaiana, G. S. 1978, ApJ, 220, 643

Schou, J., Scherrer, P. H., Bush, R. I., et al. 2012, Sol. Phys., 275, 229

Schrijver, C. J. 1983, A&A, 127, 289

Schrijver, C. J. 1987, A&A, 172, 111
Spitzer, L. 1962, Physics of Fully Ionized Gases (2nd edition (New York: Interscience))
Testa, P., Saar, S. H., & Drake, J. J. 2015, Philosophical Transactions of the Royal Society of London Series A, 373, 20140259
Tomczyk, S., McIntosh, S. W., Keil, S. L., et al. 2007, Science, 317, 1192
van Ballegooijen, A. A., Asgari-Targhi, M., Cranmer, S. R., & DeLuca, E. E. 2011, ApJ, 736, 3
Vidotto, A. A., Gregory, S. G., Jardine, M., et al. 2014, MNRAS, 441, 2361
Warnecke, J. & Bingert, S. 2020, Geophysical and Astrophysical Fluid Dynamics, 114, 261
Warnecke, J. & Peter, H. 2019a, A&A, 624, L12
Warnecke, J. & Peter, H. 2019b, arXiv e-prints, arXiv:1910.06896
Withbroe, G. L. & Noyes, R. W. 1977, ARA&A, 15, 363
Zhuleku, J., Warnecke, J., & Peter, H. 2020, A&A, 640, A119